Improvements and mechanisms of fracture and fatigue properties of well-dispersed alumina/epoxy nanocomposites

Su Zhao [a,*], Linda S. Schadler [a], Henrik Hillborg [b], Tommaso Auletta [b]

[a] *Department of Materials Science and Engineering and Rensselaer Nanotechnology Center, Rensselaer Polytechnic Institute, 110 8th Street, Troy, NY 12180, USA*
[b] *ABB Corporate Research, Forskargränd, 7721 78, Västerås, Sweden*

ABSTRACT

In an earlier paper [Zhao S, Schadler LS, Hillborg H, Auletta T, Duncan R. Mechanisms leading to improved mechanical performance in nanoscale alumina filled epoxy. Compos Sci Technol 2008], a model system of nanoscale alumina filled bisphenol A based epoxy with two interface conditions was used to highlight the mechanisms leading to significant improvements in ductility, tensile toughness and modulus. In this paper, the fracture toughness and fatigue crack propagation (FCP) rate of the materials used in the preceding paper were measured as a function of interface condition to gain further insight into the mechanisms leading to enhanced mechanical performance. No significant improvement in fracture toughness or fracture energy was observed. A significant improvement in FCP resistance was observed for both nanocomposites, but the improvement was larger for the composites with a stronger particle/matrix interface. The crack arresting mechanisms include particle matrix debonding, plastic void growth, and in the nanocomposites with a stronger interface, significant plastic deformation of the matrix around the well-bonded nanoparticles.

© 2008 Elsevier Ltd. All rights reserved.

1. Introduction

In the preceding paper [1], the mechanisms leading to enhanced ductility in nanoscale alumina/epoxy matrices was reported. Two interface conditions were investigated: the nascent interface, which lead to a weak interface, and a silane modified interface with covalent bonding to the epoxy. Particle debonding, plastic void growth and crack deflection were present in both composites, but both plastic void growth and crack deflection were more prevalent for the stronger interface condition. In this paper, the fracture and fatigue crack propagation behavior of the nanocomposites were studied in order to gain further insight into the mechanisms leading to improved mechanical performance.

Brittle epoxies are often toughened using micron-sized soft rubber particles or rigid particles [2–6]. However the stiffness or ductility is often reduced due to the addition of the soft or rigid fillers. Recently, nanosized fillers have been shown to increase toughness, modulus, and ductility simultaneously [7–10]. There have been several reports of improved ductility and toughness in brittle thermoset polymers due to the addition of equiaxed nanoparticles. Kinloch et al. [11] showed that the addition of a low concentrations of nanosilica (SiO$_2$) particles to a typical rubber-toughened epoxy, based upon a two-part epoxy formulation, lead to a significant increase in the fracture toughness or energy (K_{Ic} or G_{Ic}) of the resin. In

addition [12], the value of G_{Ic} increased from 103 J/m^2 for the pure epoxy polymer to over 1400 J/m^2 upon the formation of the 'hybrid' material containing both rubbery micron-sized particles and nano-SiO$_2$ particles in a hot-cured single-part epoxy. Plastic deformation of the matrix, crack deflection and twisting around particles, and crack front pinning by rigid particles were the main toughening mechanisms of this 'hybrid' epoxy polymer. Johnsen et al. [13] reported that the fracture toughness, K_{Ic}, increased significantly for nanosilica filled epoxy compared with the neat polymer. They reported that the primary toughening mechanism was plastic void growth. Wetzel et al. [14] showed that the fracture toughness, K_{Ic}, of nanoalumina filled epoxy composite increased by 60% at a filler content of 5 vol.%; the FCP resistance of the nanocomposites also improved. They attributed the improvement to crack deflection, plastic deformation and crack pinning. More recently, Blackman et al. [15] reported a significant improvement in both the initial toughness, K_{Ic}, and the cyclic-fatigue behavior, threshold ΔK_{th}, of the epoxy by introducing nanosilica. This result is noteworthy, however the mechanism leading to the improvement of the fatigue behavior was not mentioned.

The different mechanisms observed by these authors may be due to differences in the strength of the interface between the nanoparticles and the matrix. The relationship between the strength of the interface for nanoscale fillers and toughening mechanisms is not well understood. This paper attempts to clarify the mechanisms operating in nanofilled composite for two interface conditions. The strong interface was achieved by silane surface

* Corresponding author. Tel.: +1 518 276 3011; fax: +1 518 276 6540.
E-mail address: su.zhao.rpi@gmail.com (S. Zhao).

treatment of the nanoparticles, however the untreated nanoparticles led to the weak interface.

2. Experimental

2.1. Materials and sample preparation

The same materials used in the preceding paper [1] were used here, including a Huntsman Araldite® epoxy, NanoTek® aluminum oxide nanoparticles (45 nm, determined from specific surface area, Nanophase Technologies Corporation), and silane coupling agent (3-aminopropyltriethoxysilane (APTES), Gelest Inc.). The nanoparticle size distribution was examined by TEM (not shown here), with the range from 20 to 200 nm. The silane surface treatment method and the nanocomposites preparation procedure were also introduced in the preceding paper [1].

2.2. Fracture toughness test

Compact tension (CT) specimens were used to determine the fracture toughness, K_{Ic}, at the onset of crack growth of the materials. Specimens were molded from silicone rubber and polished before using. The fracture toughness of the materials was determined by means of CT tests on at least four specimens according to ASTM Standard E1820 and ASTM Standard D5045. CT specimens were tested under displacement control on an Instron 4204 machine, using pin loading and a low deformation speed of 0.1 mm/min. At least 4 samples were tested for each condition. The thickness B and the width W of specimens were chosen to be 12.7 and 25.4 mm, respectively. Prior to testing, a notch was molded and then sharpened by tapping a fresh razor blade in to the material, so that a sharp crack was initiated with a length a_0 between 0.45 and 0.55 W. The initial crack length a_0 was determined on fracture surfaces using optical microscopes (Olympus BH-2 and SZX12) with Color View soft imaging systems. The tests were computer controlled using LabView software. The samples were tested to failure, and the fracture toughness K_{Ic} was calculated based on the formula provided in ASTM D5045. The value of the fracture energy, G_{Ic}, was then calculated from

$$G_{Ic} = \frac{K_{Ic}^2}{E}(1 - v^2) \tag{1}$$

Where E is the Young's modulus taken from tensile results [1], v is the Poisson's ratio of the polymer, taken to be 0.35 [13,24].

2.3. Fatigue crack growth rate test

The tapered double-cantilever beam (TDCB) specimen geometry with side grooves was used to measure the fatigue crack growth rate of the materials [25]. The TDCB fracture specimen, developed by Mostovoy et al. [26] and modified by Beres et al. [27] gives a constant stress intensity factor K_I during fatigue test. The geometry and design of the TDCB specimen used in this work were introduced by Brown et al. [28,29]. The fatigue crack growth rate tests were performed on the Instron 8562 machine with a 5 kN load cell. The samples were pin loaded. The fatigue crack lengths were measured optically by a Hitachi Digital Signal Processor (DSP) – VK-370 color video camera with a canon lens on a self-made traveler. A black-and-white TV was used to monitor the crack growth and the video data were captured through a computer every 5 s. The TDCB geometry provides a crack-length-independent relationship between applied stress intensity factor K_I and load P for crack lengths ranging from 20 to 40 mm [25,29]. Therefore a constant range of Mode-I stress intensity factor ΔK_I was achieved by applying a constant range of load ΔP independent of crack length (crack length between 20 and 40 mm). A triangle frequency of 1 Hz was applied with a load ratio ($R = K_{min}/K_{max}$) of 0.1. The fatigue crack growth rate da/dN was then calculated from the fatigue crack length captured by the video camera at different stress intensity ranges ΔK_I. Several ΔK_I were applied to each sample by varying the load and at least four samples were tested for each material. TDCB specimens were pre-cracked with a fresh razor blade before testing. The log–log plot of fatigue crack growth rate da/dN vs. the applied range of stress intensity factors ΔK_I was then determined and fit to the Paris law [30].

$$\frac{da}{dN} = C_0 \Delta K_I^n \tag{2}$$

Where a is the crack length, N is the number of cycles, da/dN is the fatigue crack growth rate and C_0 and n are Paris Law constants.

2.4. Fracture surface properties

The surface roughness of the K_{Ic} test fracture surfaces was measured at the University of Florida using a Dektak® 8 Advanced Development Profiler from Veeco Instruments Inc. 2D scans were performed by this stylus profilometer with a 12.5 μm needle. At least 10 scan were performed for each material at different positions and the average roughness were calculate from the scanning data by the Dektak® 8 software.

A JEOL 6330F Field Emission Scanning Electron Microscope (FE-SEM) and a JEOL CM12 Transmission Electron Microscope (TEM) were used to observe the dispersion of nanoparticles and the morphology of fracture surfaces of the K_{Ic} test and fatigue crack growth rate test samples.

3. Results

3.1. Dispersion of nanocomposites

Good dispersion is critical for taking advantage of nanoscale particles and obtaining optimized properties. Fig. 1 shows the dispersion in the NT-Al$_2$O$_3$ and APTES-Al$_2$O$_3$ nanocomposites; many of the nanoparticles were individually dispersed. Only a few aggregates (approximately 4–8) with a diameter of 2–6 μm on the 3×3 mm cross-section of each nanocomposite were observed (not shown here). A comparison of Fig. 1(b) and (d) show that the nanoparticle/epoxy adhesion was stronger for the APTES-Al$_2$O$_3$ nanocomposites, which was due to the surface treatment of Al$_2$O$_3$ nanoparticles by APTES silane.

3.2. Fracture toughness and energy

The fracture toughness and fracture energy values of the neat polymer, NT-Al$_2$O$_3$ and APTES-Al$_2$O$_3$/epoxy nanocomposites are shown in Table 1. It is clear that although the fracture toughness of both nanocomposites increased with the nanofiller content, the K_{Ic} values of the APTES-Al$_2$O$_3$/epoxy nanocomposites are slightly higher than that of the NT-Al$_2$O$_3$/epoxy nanocomposites through the whole filler loading range. However, t-test results show that the improvements in fracture toughness, K_{Ic}, are not significant. The fracture energy of the APTES-Al$_2$O$_3$/epoxy nanocomposites, however, which includes the Young's modulus, did show a significant increase was optimized around 10–15 phr nanoparticle loading. There was, however, no significant change for the NT-Al$_2$O$_3$/epoxy nanocomposites.

3.3. Fatigue crack propagation behavior

Fig. 2 shows a log-log plot of fatigue crack growth rate (da/dN) vs. applied stress intensity range (ΔK_I) for the neat polymer, 10 phr NT-
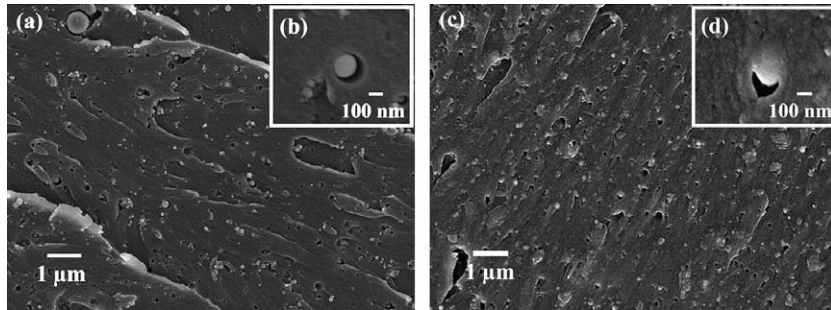
Fig. 1. Scanning Electron Micrographs showing the nanoparticle dispersion in (a) and (b) 10 phr NT-Al$_2$O$_3$ nanocomposites, and (c) and (d) 10 phr APTES-Al$_2$O$_3$ nanocomposites.

Table 1
Fracture properties for the neat polymer, NT-Al$_2$O$_3$ and APTES-Al$_2$O$_3$/epoxy nanocomposites

Materials	Amount of Al$_2$O$_3$		K_{Ic}		E	G_{Ic}	
	phr	vol.%	MPa m$^{1/2}$	Rel. change (%)	GPa	J/m^2	Rel. change (%)
Neat polymer	–	0	0.94 ± 0.07	–	3.42 ± 0.1	227 ± 16.9	–
NT-Al$_2$O$_3$/epoxy nanocomposites	5	1.6	1.00 ± 0.05	6.4	3.70 ± 0.1	237 ± 11.9	4.4
	10	3.1	1.03 ± 0.04	9.6	3.90 ± 0.1	239 ± 9.3	5.3
	15	4.6	1.05 ± 0.07	11.7	3.99 ± 0.1	242 ± 16.1	6.6
	20	6.1	1.03 ± 0.04	9.6	4.03 ± 0.1	230 ± 8.9	1.3
APTES-Al$_2$O$_3$/epoxy nanocomposites	5	1.6	1.02 ± 0.02	8.5	3.48 ± 0.1	262 ± 5.1	15.4
	10	3.1	1.09 ± 0.06	16.0	3.64 ± 0.1	286 ± 15.7	26.0
	15	4.6	1.10 ± 0.07	17.0	3.71 ± 0.1	286 ± 18.2	26.0
	20	6.1	1.08 ± 0.06	14.9	3.88 ± 0.1	264 ± 14.7	16.3

± : Standard deviation.

Al$_2$O$_3$ and 10 phr APTES-Al$_2$O$_3$/epoxy nanocomposites. The lines indicate a linear relationships described by the empirical Paris Law equation (Eq. (2)). A transition point, at $\Delta K_T = 0.27$ MPa $\sqrt{m}$, is observed. At this point, the FCP resistance of all three materials is about the same. This behavior is similar to that observed in some rubber particle filled epoxy [31], in which rubber cavitation and matrix dilation only occur above certain ΔK_I values. The observation of this transition point in our nanocomposites may indicate that the operating mechanisms are different for ΔK_I levels below and above ΔK_T. Above this transition point, the enhancement brought about by the nanoparticles is clear and very significant improvements in reducing the crack growth rate can be clearly seen: (i) The fatigue crack growth rate increases more slowly with applied stress intensity range for both the nanocomposites than for the neat polymer; (ii) the APTES-Al$_2$O$_3$/epoxy nanocomposite shows the highest FCP resistance compared to the other two materials at the same ΔK_I va-

lue. In addition, the Paris Law constant C_0 and n are calculated by curve fitting and are listed in Table 2.

Both a smaller C_0 and a smaller n indicate a retardation of the crack growth rate. The value of the Paris law exponent n drops from 10 for the pure epoxy to 7 for 10 phr (3.1 vol.%) NT-Al$_2$O$_3$/epoxy nanocomposites, and further to 5 for 10 phr (3.1 vol.%) APTES-Al$_2$O$_3$/epoxy nanocomposites. Azimi et al. [31] reported that the Paris law exponent n decreased from 9.0 for the neat epoxy to 6.8 for 10 vol.% glass microcapsules and 4.9 for 10 vol.% rubber microparticles. This result indicates that we achieved the same fatigue crack propagation resistance at smaller filler content for the nanocomposites. In addition, the value of the intercept C_0 drops from 42.1×10^{-3} (mm/cycle(MPa $\sqrt{m}$)^n) for pure epoxy to 0.39×10^{-3} (mm/cycle(MPa $\sqrt{m}$)^n) for 10 phr NT-Al$_2$O$_3$/epoxy nanocomposites, and further to 0.07×10^{-3} (mm/cycle(MPa $\sqrt{m}$)^n) for 10 phr APTES-Al$_2$O$_3$/epoxy nanocomposites. All of these results show that fatigue crack propagation in the epoxy is impeded by the Al$_2$O$_3$ nanoparticles; furthermore, this effect is stronger for the surface treated APTES-Al$_2$O$_3$ nanoparticles than the NT-Al$_2$O$_3$ nanoparticles.

3.4. Fracture morphology

The K_{Ic} fracture surface morphologies for the neat polymer, NT-Al$_2$O$_3$ and APTES-Al$_2$O$_3$/epoxy nanocomposites are shown in Fig. 3(a), (b), (c), (d) and (e), respectively. All crack propagation is
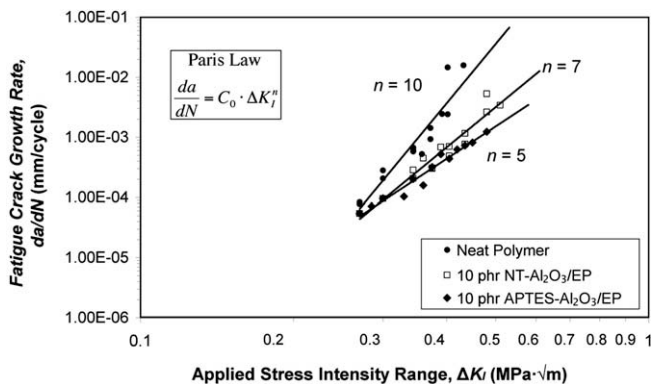

Fig. 2. Log-log plot of fatigue crack growth rate (da/dN) vs. applied stress intensity rang (ΔK_I) for neat polymer, 10 phr NT-Al$_2$O$_3$ and 10 phr APTES-Al$_2$O$_3$/epoxy nanocomposites. The lines indicate the linear relationships.

Table 2
Paris Law constant C_0 and n for neat polymer, 10 phr NT-Al$_2$O$_3$ and 10 phr APTES-Al$_2$O$_3$/epoxy nanocomposites

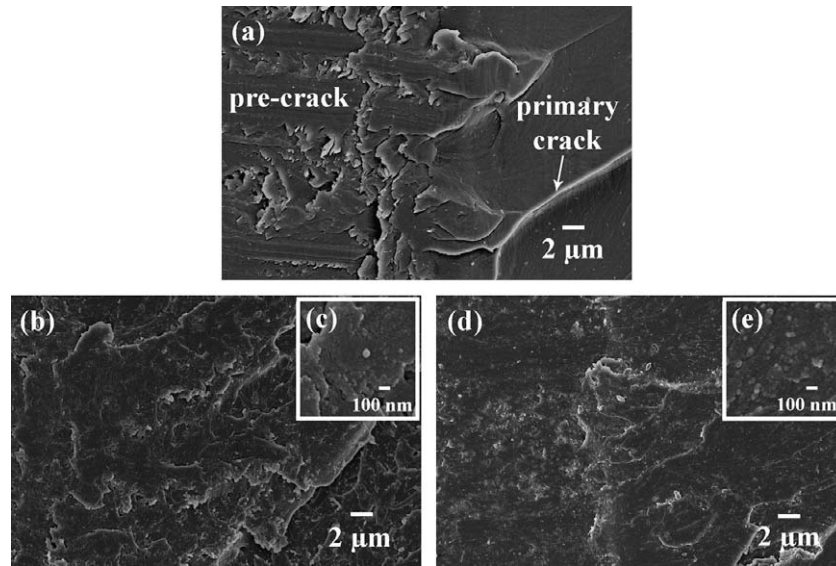| Materials	C_0 (mm/cycle(MPa $\sqrt{m}$)^n)	n
Neat polymer	42.1×10^{-3}	10
10 phr NT-Al$_2$O$_3$/epoxy nanocomposites	0.39×10^{-3}	7
10 phr APTES-Al$_2$O$_3$/epoxy nanocomposites	0.07×10^{-3}	5

Fig. 3. Fracture surface morphology after K_{Ic} test for (a) neat polymer, (b) and (c) 10 phr NT-Al$_2$O$_3$/epoxy nanocomposite, and (d) and (e) 10 phr APTES-Al$_2$O$_3$/epoxy nanocomposite.

from left to right. The structure at the left end of each material is from the pre-crack made by a fresh razor blade. In the neat polymer, large, straight primary cracks with a smooth region in between are seen (Fig. 3(a)). This indicates that once the stress intensity factor K reaches its critical value K_{Ic}, the crack propagates very fast and straight until failure. The fracture surfaces of the NT-Al$_2$O$_3$ and APTES-Al$_2$O$_3$/epoxy nanocomposites are quite similar (Fig. 3(b) and (d)). It is clear that both the 10 phr NT-Al$_2$O$_3$ and 10 phr APTES-Al$_2$O$_3$/epoxy nanocomposites have a rougher fracture surface, indicating increased surface roughness as a result of adding nanoparticles. Debonding and plastic void growth, which were the mechanisms observed on the tensile test fracture surfaces of the nanocomposites at high magnification [1], are not seen here (Fig. 3(c) and (e)).

The fracture morphology of the fatigue crack growth rate (FCGR) test samples close to the pre-crack position for the neat polymer, 10 phr NT-Al$_2$O$_3$ and 10 phr APTES-Al$_2$O$_3$/epoxy nano-

composites are shown in Fig. 4. The crack propagation direction is indicated by the white arrow. The fracture morphologies near the pre-crack of the FCGR test samples (Fig. 4) are quite similar to that of the K_{Ic} test samples (Fig. 3). In the neat polymer, straight primary cracks can be seen once the crack starts propagating (Fig. 4(a)). In the 10 phr NT-Al$_2$O$_3$ and 10 phr APTES-Al$_2$O$_3$/epoxy nanocomposites, small secondary cracks and detailed structures are observed (Fig. 4(b) and (c)).

Away from the pre-crack position, the fatigue cracks propagate during cyclic stresses; therefore fatigue striations should be observed. Fig. 5 shows the fatigue striations on a FCGR test sample for the neat polymer (applied $\Delta K_I \sim 0.5$ MPa $\sqrt{m}$). The crack growth direction is from the right-up comer to the left-bottom comer. Big branch marks can be observed, which are indicative of the brittle nature of epoxy.

The situation for the nanocomposites is quite different from the neat polymer. Fig. 6 shows the fatigue morphology of a FCGR test
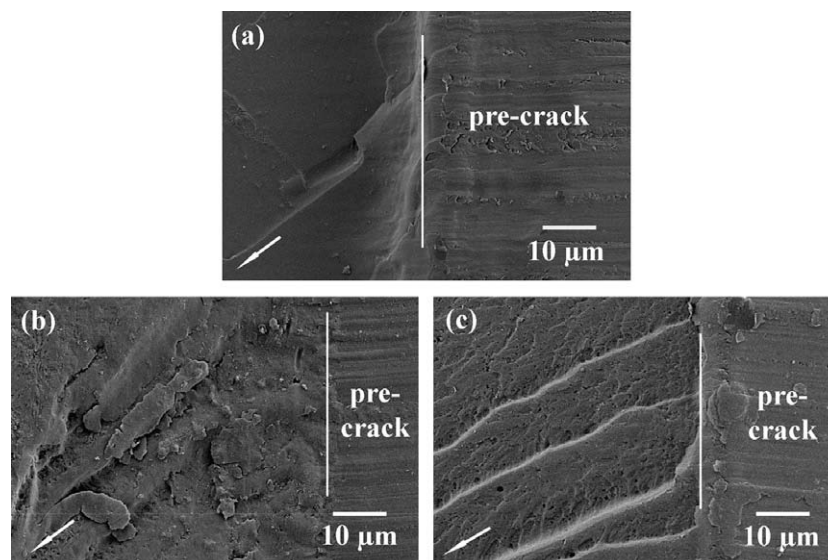

Fig. 4. Fracture morphology of the FCGR test samples close to the pre-crack position for (a) neat polymer, (b) 10 phr NT-Al$_2$O$_3$ and (c) 10 phr APTES-Al$_2$O$_3$/epoxy nanocomposites. White arrow indicates the crack propagation direction.
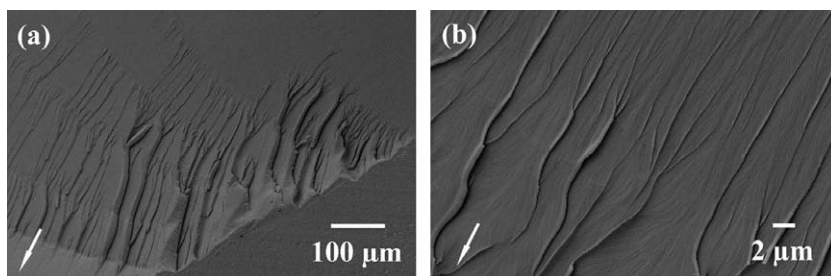
Fig. 5. Fracture striations on a FCGR test sample for neat polymer. White arrow indicates the crack propagation direction (applied $\Delta K_1 \sim$0.5 MPa $\sqrt{m}$).

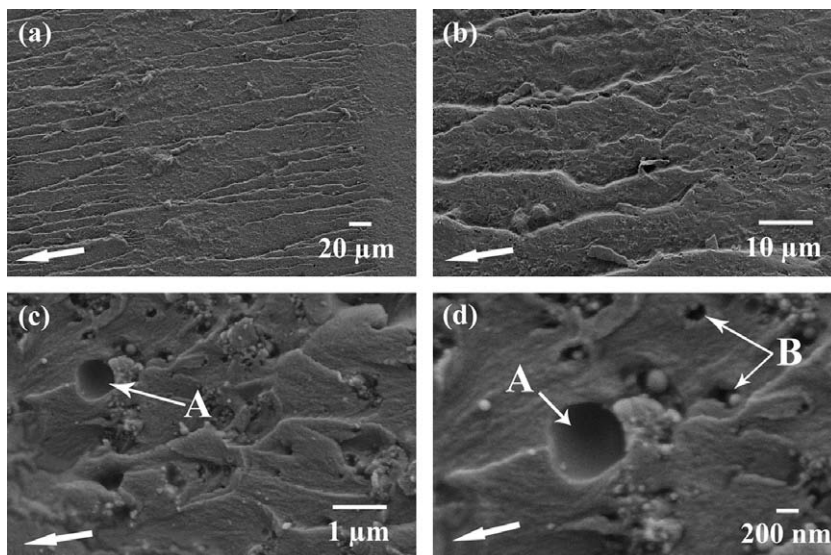**Fig. 6.** Fracture striations on a FCGR test sample for 10 phr NT-Al$_2$O$_3$/epoxy nanocomposite (applied $\Delta K_1 \sim$0.5 MPa $\sqrt{m}$). Mechanisms: A, particle pull-out; B, debonding and plastic void growth. White arrow at left-bottom corner indicates the crack propagation direction.

sample for the 10 phr NT-Al$_2$O$_3$ nanocomposite at different magnifications. Fatigue striations are still clear (Fig. 6(a)). With increasing magnification, however, more river lines, debonding, plastic void growth and particle pull-out mechanisms can be seen (Fig. 6(c) and (d)). We observed these mechanisms for the NT-Al$_2$O$_3$/epoxy nanocomposites in a low crack-propagation-speed tensile test [1], but not for the high crack-propagation-speed fracture toughness test. In the present low frequency fatigue test, the applied stress intensity range is only about 1/3 to 1/2 of the K_{Ic} value, and the crack propagation rate is much lower than in the fracture toughness test. Therefore the crack propagation speed, not surprisingly, also impacts the operating mechanism.

Fig. 7 shows the fatigue striation morphology on a FCGR test sample for the 10 phr APTES-Al$_2$O$_3$ nanocomposite at different magnifications. More river lines, debonding and plastic void growth, and particle pull-out mechanisms can also be seen here. In addition, some new features are presented. Unique 3D plastic deformation of the matrix around the nanoparticles can be clearly observed. The well-bonded APTES-Al$_2$O$_3$ nanoparticles or small aggregates of few nanoparticles act as pinning positions and induce plastic deformation of the matrix during the low crack-propagation-rate fatigue test. This mechanism makes it possible to further retard the fatigue crack growth rate of the epoxy matrix.

4. Discussion

The possible fracture and fatigue mechanisms, including crack deflection [16–19], crack pinning [20–22], debonding [23] and

plastic void growth [4,13], and plastic deformation of the matrix are discussed in the following section.

4.1. Crack deflection

An increase in fracture surface roughness can be used as evidence to prove crack deflection occurs, which is associated with an increase in the crack length and therefore the energy absorbed during deformation [32,33]. However the fracture surface roughness of both NT-Al$_2$O$_3$ and APTES-Al$_2$O$_3$/epoxy nanocomposites did not change significantly compared with the neat polymer (not shown here). In addition, the fracture surface roughness values of all materials from the K_{Ic} fracture toughness test are much smaller compared to that from the tensile test (Fig. 8 in [1]). This result implies that crack deflection is more prevalent in the tensile test environment than in the pre-cracked fracture toughness test. This is because in the fracture toughness test, a sharp pre-crack with crack length a_0 has been produced by a fresh razor blade before testing, which gives a much higher stress intensity value K at the crack tip than in the nominally defect free tensile test at the same applied stress condition. During the pre-cracked fracture toughness test, the K value reaches the K_{Ic} value very fast and the stored energy is dissipated by high-speed unstable crack growth and leaves a smooth fracture surface [36]. On the contrary, in the tensile test, the crack grows very slowly after initiation; then cracks accelerate and any excess energy is dissipated by driving the crack faster (the 'mirror' zone); outside the mirror zone, the crack reaches its limiting speed, and excess stored energy is dissipated in
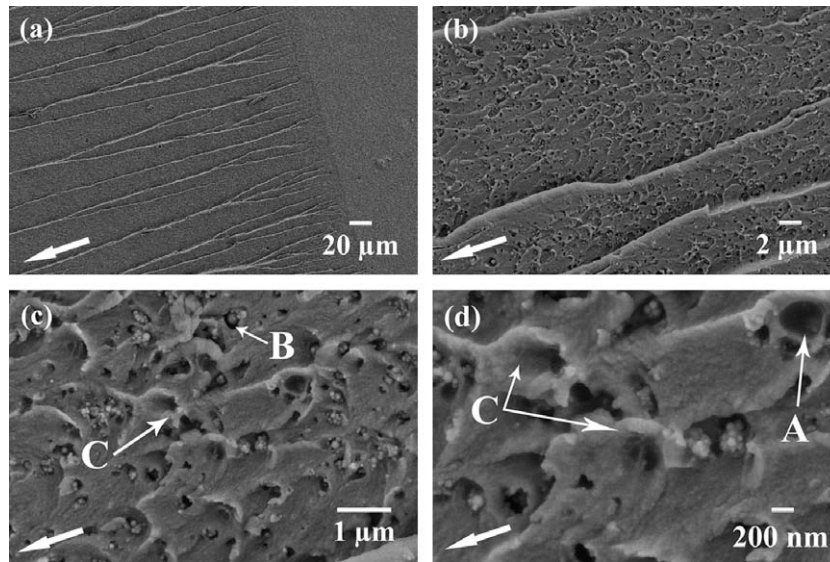
Fig. 7. Fracture striations near the center of width on a FCGR test sample for 10 phr APTES-Al$_2$O$_3$/epoxy nanocomposite (applied $\Delta K_1 \sim$0.5 MPa $\sqrt{m}$). Mechanisms: A, particle pull-out; B, debonding and plastic void growth; C, plastic deformation of matrix. White arrow at left-bottom corner indicates the crack propagation direction.

bifurcation and leaves a rough 3D fracture surface (the 'rough' zone) [36].

Work by Arakawa and Takahashi [37], as reported by Hull [32,33], showed that the toughening effect due to an increase in true fracture surface area from crack deflection gives a linear relationship between the surface roughness and the fracture energy. However no such correlation exists for these nanocomposites (Fig. 8). Fracture energy was the highest at 10–15 phr for both the NT-Al$_2$O$_3$ and the APTES-Al$_2$O$_3$/epoxy nanocomposites, but the roughness increased linearly with loading. This result indicates that the small increases of surface roughness for the nanocomposites may not be due to the crack deflection. In addition, the plot of surface roughness vs. fracture toughness is shifted to the right for the APTES-Al$_2$O$_3$/EP compared to the NT-Al$_2$O$_3$ implying that while surface roughness may play a part, it is not a primary mechanism.

In addition to surface roughness, Faber and Evans' crack deflection theory [16,17] can be used to predict the increases in fracture energy G_{Ic}. However, Evans' theory states that crack deflection will occur when the obstacle dimension is larger than the plastic zone, which is not the case in the present work. This and the surface roughness results discussed above indicate that crack deflection is not the main toughening mechanism.
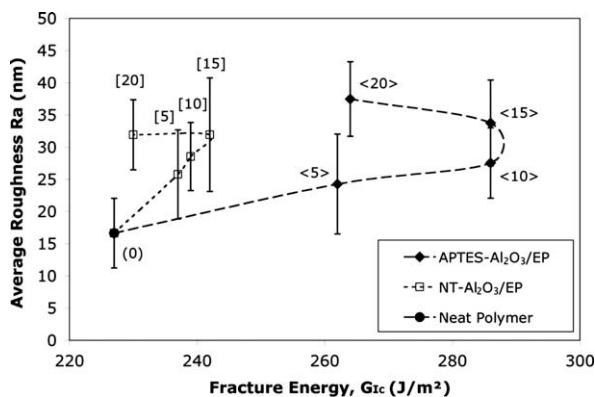

Fig. 8. Correlation between fracture surface roughness Ra and fracture energy G_{Ic} for the neat polymer, NT-Al$_2$O$_3$ and APTES-Al$_2$O$_3$/epoxy nanocomposites; numbers in parentheses represent the nanoparticle concentration (phr).

4.2. Crack pinning

According to crack pinning theory by Evans [21] and by Green et al. [22], the predicted σ_c/σ_m ratio (the ratio of the stress required to propagate a crack in the composite to the stress required for a crack in pure matrix) and the experimental σ_c/σ_m ratio calculated from the ratio of fracture toughness $K_{Ic}/K_{Ic,m}$ did not correlate (not shown here), indicating that crack pinning is not a primary toughening mechanism.

4.3. Debonding and plastic void growth

The prediction by Evans' model and the experimental data of the fracture energy increment $G_{Ic}/G_{Ic,m}$ were compared (not shown). The experimental data points fell far below the prediction line, indicating that debonding in the plastic zone ahead of the pre-crack tip is unlikely for both of the nanocomposites under K_{Ic} fracture toughness test conditions. This result corresponds to the fracture morphology of the K_{Ic} samples. No debonding and plastic void growth or particle pull-out were observed for the high crack-propagation-speed K_{Ic} test fracture surfaces for both NT-Al$_2$O$_3$ and APTES-Al$_2$O$_3$/epoxy nanocomposites (Fig. 3(c) and (e)). However, debonding, plastic void growth and particle pull-out were clearly seen in both nanocomposites on the low crack-propagation-speed fatigue test fracture surfaces (Fig. 6(c) and (d) and, Fig. 7(c) and (d)), because debonding and plastic void growth are crack propagation speed dependent.

4.4. Plastic deformation of the matrix

3D plastic deformation of the matrix around the well-bonded nanoparticles was only seen on the fatigue test fracture surfaces of the APTES-Al$_2$O$_3$/epoxy nanocomposite (Fig. 7). This extra mechanism helps further retard the fatigue crack growth rate of the APTES-Al$_2$O$_3$/epoxy nanocomposite compared to the NT-Al$_2$O$_3$/epoxy nanocomposite (Fig. 2). As discussed above, on the K_{Ic} test fracture surfaces of the NT-Al$_2$O$_3$/epoxy and the APTES-Al$_2$O$_3$/epoxy nanocomposites, there is no difference in the degree of crack deflection; there is less evidence of debonding or plastic void growth; therefore plastic deformation of the matrix, due to the surface modification of the nanoparticles in the APTES-Al$_2$O$_3$/epoxy

nanocomposite, might be one explanation for the extra increment in its fracture energy (Fig. 8).

5. Conclusions

The fracture toughness and fatigue crack growth rate of well-dispersed Al_2O_3/epoxy nanocomposites were measured as a function of nanoparticle loading and particle/matrix compatibility. The main conclusions are:

(1) To improve the fracture energy of nanocomposites compared to unfilled resin, a stronger interface is helpful. The NT-Al_2O_3/epoxy nanocomposites with a weaker interface did not show an improvement in fracture energy compared to the neat polymer. The APTES-Al_2O_3/epoxy nanocomposites with a stronger interface exhibited a significant increase in fracture energy at 10–15 phr.
(2) Crack deflection is not the main mechanism for the increment in fracture energy of both nanocomposites. However, plastic deformation of the matrix might explain the extra increment in fracture energy of the APTES-Al_2O_3/epoxy nanocomposites.
(3) Debonding and plastic void growth as well as plastic deformation of the matrix were found to be the key mechanisms leading to improved fatigue crack resistance.
(4) Significant plastic deformation can occur in epoxy when the crack propagation speed is slow (fatigue tests) and the particle/matrix bonding is high as in the case of APTES-Al_2O_3/epoxy nanocomposites

References

[1] Zhao S, Schadler LS, Hillborg H, Auletta T, Duncan R. Mechanisms leading to improved mechanical performance in nanoscale alumina filled epoxy. Compos Sci Technol 2008;68:2965–75.
[2] Bucknall CB. Toughened plastics. London: Applied Science Publishers; 1977.
[3] Pearson RA, Yee AF. Influence of particle size and particle size distribution on toughening mechanisms in rubber-modified epoxies. J Mater Sci 1991;26:3828–44.
[4] Huang Y, Kinloch AJ. Modelling of the toughening mechanisms in rubber-modified epoxy polymers. J Mater Sci 1992;27:2763–9.
[5] Liang JZ, Li RKY. Rubber toughening in polypropylene: a review. J Appl Polym Sci 2000;77:409–17.
[6] Kinloch AJ, Young RJ. Fracture behaviour of polymers. Elsevier Applied Science; 1983.
[7] Ajayan PM, Schadler LS, Braun PV. Nanocomposite science and technology. 1st ed. Wiley-VCH; 2003.
[8] Rong MZ, Zhang MQ, Zheng YX, Zeng HM, Walter R, Friedrich K. Structure–property relationships of irradiation grafted nano-inorganic particle filled polypropylene composites. Polymer 2001;42(1):167–83.
[9] Naous W, Yu X, Zhang Q, Naito K, Kagawa Y. Morphology, Tensile properties, and fracture toughness of epoxy/Al_2O_3 nanocomposites. J Polym Sci B Polym Phys 2006;44:1466–73.
[10] Xu Y, Chung DDL, Mroz C. Thermally conducting aluminum nitride polymer-matrix composites. Composites Part A 2001;32:1749–57.
[11] Kinloch AJ, Lee JH, Taylor AC, Sprenger S, Eger C, Egan D. Toughening structural adhesives via nano- and micro-phase inclusions. J Adhes 2003;79:867–73.
[12] Kinloch AJ, Mohammed RD, Taylor AC, Eger C, Sprenger S, Egan D. The effect of silica nano particles and rubber particles on the toughness of multiphase thermosetting epoxy polymers. J Mater Sci 2005;40:5083–6.
[13] Johnsen BB, Kinloch AJ, Mohammed RD, Taylor AC, Sprenger S. Toughening mechanisms of nanoparticle-modified epoxy polymers. Polymer 2007;48:530–41.
[14] Wetzel B, Rossso P, Haupert F, Friedrich K. Epoxy nanocomposites – fracture and toughening mechanisms. Eng Fract Mech 2006;73:2375–98.
[15] Blackman BRK, Kinloch AJ, Sohn Lee J, Talor AC, Agarwal R, Schueneman G. The fracture and fatigue behaviour of nano-modified epoxy polymers. J Mater Sci 2007;42:7049–51.
[16] Faber KT, Evans AG. Crack deflection process – I. Theory. Acta Metall 1983;31:565–76.
[17] Faber KT, Evans AG. Crack deflection process – II. Experiment. Acta Metall 1983;31:577–84.
[18] Spanoudakis J, Young RJ. Crack propagation in a glass particle-filled epoxy resin. Part 1 – effect of particle volume fraction and size. J Mater Sci 1984;19:473–86.
[19] Spanoudakis J, Young RJ. Crack propagation in a glass particle-filled epoxy resin. Part 2 – effect of particle-matrix adhesion. J Mater Sci 1984;19:487–96.
[20] Lange FF. The interaction of a crack front with a second-phase dispersion. Philos Mag 1970;22:983–92.
[21] Evans AG. The strength of brittle materials containing second phase dispersions. Philos Mag 1972;26:1327–44.
[22] Green DJ, Nicholson PS, Embury JD. Fracture of a brittle particulate composite. Part 2 – theoretical aspects. J Mater Sci 1979;14:1657–61.
[23] Evans AG, Williams S, Beaumont PWR. On the toughness of particulate filled polymers. J Mater Sci 1985;20:3668–74.
[24] Smith RNL. Basic fracture mechanics. Oxford, UK: Butterworth-Heinemann Ltd.; 1991.
[25] Brown EN, White SR, Sottos NR. Microcapsule induced toughening in a self-healing polymer composite. J Mater Sci 2004;39:1703–10.
[26] Mostovoy S, Crosley PB, Ripling EJ. Use of crack-line loaded specimens for measuring plane-strain fracture toughness. J Mater 1967;2:661–81.
[27] Beres W, Koul AK, Thambraj R. A tapered double-cantilever-beam specimen designed for constant-K testing at elevated temperatures. J Test Eval 1997;25:536–42.
[28] Brown EN, Sottos NR, White SR. Fracture testing of a self-healing polymer composite. Exp Mech 2002;42:372–9.
[29] Brown EN. Fracture and fatigue of a self-healing polymer composite material. PhD thesis, University of Illinois at Urbana-Champaign, Department of Mechanical Engineering; 2003.
[30] Paris PC, Gomez MP, Anderson WE. A rational analytic theory of fatigue. Trends Eng Univ Washington 1961;13:9–14.
[31] Azimi HR, Pearson RA, Hertzberg RW. Fatigue of hybrid epoxy composites: epoxies containing rubber and hollow glass spheres. Polym Eng Sci 1996;36:2352–65.
[32] Hull D. Fractography – observing, measuring and interpreting fracture surface topography. Cambridge University Press; 1999.
[33] Hull D. Influence of stress intensity and crack speed on fracture surface topography: mirror to mist to macroscopic bifurcation. J Mater Sci 1996;31:4483–92.
[36] Roulin-Moloney AC. Fractography and failure of mechanisms of polymers and composites. Elsevier Applied Science; 1989.
[37] Arakawa K, Takahashi K. Relationships between fracture parameters and fracture surface roughness of brittle polymers. Int J Frac 1991;48:103–14.